

1 **Article type:** Research paper

2

3 **Nitrogen-carbon graphite-like semiconductor synthesized from uric acid**

4

5 Roberto C. Dante^{1*}, Pedro Chamorro-Posada², José Vázquez-Cabo³, Óscar Rubiños-
6 López³, Francisco M. Sánchez-Árevalo⁴, Lázaro Huerta⁴, Pablo Martín-Ramos⁵, Luis
7 Lartundo-Rojas⁶, Carlos F. Ávila-Vega⁷, Edgar D. Rivera-Tapia⁸, Cristian A. Fajardo-
8 Pruna⁹, Álvaro J. Ávila-Vega¹⁰ and Omar Solorza-Feria¹¹

9

10 ¹ Research, Development & Innovation, 2Dto3D S.r.l.s. Via Revalanca 5, 12036 San
11 Firmino, Revello (CN), Italy.

12 ² Dpto. de Teoría de la Señal y Comunicaciones e IT, Universidad de Valladolid, ETSI
13 Telecomunicación, Paseo Belén 15, 47011 Valladolid, Spain.

14 ³ Dpto. de Teoría de la Señal y Comunicaciones, Universidad de Vigo, ETSI
15 Telecomunicación, Lagoas Marcosende s/n, Vigo, Spain.

16 ⁴ Instituto de Investigaciones en Materiales, Universidad Nacional Autónoma de
17 México, Apdo. Postal 70-360, Cd. Universitaria, Mexico City 04510, Mexico.

18 ⁵ EPS, Universidad de Zaragoza, Carretera de Cuarte s/n, 22071, Huesca, Spain.

19 ⁶ Instituto Politécnico Nacional, Centro de Nanociencias y Micro y Nanotecnologías de
20 Nanociencias, UPALM, Zacatenco, Mexico City, 07738, Mexico.

21 ⁷ Departamento de Ingeniería Civil y Ambiental, Escuela Politécnica, Escuela
22 Politécnica Nacional (EPN), Ladrón de Guevara E11 - 253. Quito, Ecuador.

23 ⁸ Newcastle University, School of Mechanical Engineering, Newcastle upon Tyne NE1
24 7RU, UK.

* Corresponding author. Tel: +39 3407536757. E-mail: rcdante@yahoo.com

25 ⁹ Escuela Politécnica Nacional, Departamento de Formación Básica, Ladrón de
26 Guevara E11-253 Quito, Ecuador.

27 ¹⁰ Instituto Nacional de Eficiencia Energética y Energías Renovables (INER), Iñaquito
28 N3537 y Juan Pablo Saenz, Quito, Ecuador.

29 ¹¹ Departamento de Química, Centro de Investigación y de Estudios Avanzados del
30 Instituto Politécnico Nacional (CINVESTAV-IPN). Av. IPN 2508, Col. San Pedro
31 Zacatenco, Apdo. Postal 14-740, Mexico D.F. 07360, Mexico.

32

33 **Abstract**

34 A new carbon-nitrogen organic semiconductor has been synthesized by pyrolysis of uric
35 acid. This layered carbon-nitrogen material contains imidazole-, pyridine
36 (naphthyridine)- and graphitic-like nitrogen, as evinced by infrared and X-ray
37 photoelectron spectroscopies. Quantum chemistry calculations support that it would
38 consist of a 2D polymeric material held together by hydrogen bonds. Layers are stacked
39 with an interplanar distance between 3.30 and 3.36 Å, as in graphite and coke. Terahertz
40 spectroscopy shows a behavior similar to that of amorphous carbons, such as coke, with
41 non-interacting layers. This material features substantial differences from polymeric
42 carbon nitride, with some characteristics closer to those of nitrogen-doped graphene, in
43 spite of its higher nitrogen content. The direct optical band gap, dependent on the
44 polycondensation temperature, ranges from 2.10 to 2.32 eV. Although in general the
45 degree of crystallinity is low, the material synthesized at 600 °C is composed of globular
46 hollow particles, in which spots with a certain degree of crystallinity can be found.

47

48 **Keywords:** carbon nitride, nitrogen-carbon materials, organic semiconductor, THz
49 spectroscopy, uric acid

50

51 **1. Introduction**

52 The piece of work presented herein on the products obtained from the pyrolysis of uric
53 acid (UA) started with the objective to find an alternative pathway for the synthesis of
54 polymeric carbon nitride ($g\text{-C}_3\text{N}_4$), an organic semiconductor that is receiving
55 substantial attention due to its versatility and many potential applications [1-15].
56 However, the chosen precursor yielded a material with a lower nitrogen content (N to C
57 atomic ratio ~ 0.6) than that of $g\text{-C}_3\text{N}_4$ (N to C atomic ratio of 1.5) and different polymer
58 structure and electronic properties.

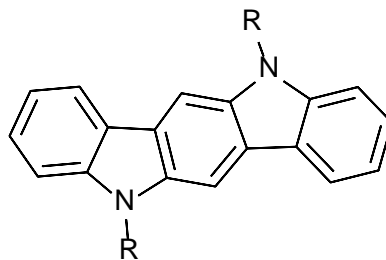
59 This novel carbon-nitrogen material would also belong to the class of organic
60 semiconductors, which combines the electronic advantages of semiconducting materials
61 with the chemical (and mechanical) benefits of organic compounds. Therefore, the
62 ability to absorb light and conduct electricity is coupled with a structure with a flexible
63 backbone that can easily be modified by chemical synthesis (however, the control of
64 modifications may depend on several factors).

65 The new synthesized material can be regarded as a graphitic material with imidazole-,
66 pyridine (naphthyridine)- and graphitic-like nitrogen. Nonetheless, whereas the
67 concentration of nitrogen in the either nitrogen-doped or defective graphite is around 2
68 or 3 at% (N to C atomic ratio of *ca.* 0.03%), the nitrogen content in this new material is
69 much higher (~ 33 at%), forcing to a less randomized distribution of defects. For
70 example, the recently synthesized C_2N exhibited a very organized 2D structure. C_2N , in
71 combination with $g\text{-C}_3\text{N}_4$, offers a potential way to improve the efficiencies of both
72 photoabsorption and electron-hole separation of $g\text{-C}_3\text{N}_4$ without involving any transition
73 metals. Fechler *et al.* synthesized nitrogen rich graphitic materials starting from various
74 types of quinones and urea as precursors, showing that the amount of nitrogen in the

75 final materials depended on reaction temperature [16-19].

76 Another extensively nitrogen-doped (mesoporous) carbon was synthesized by Goel *et*
77 *al.* from melamine and formaldehyde. They obtained an interesting cross-linked
78 structure by nanocasting that would mainly be ascribed to a certain type of melamine-
79 formaldehyde resin with a high content of bridging oxygen atoms. On the contrary, the
80 material under study has a very low content of oxygen [20]. Organic semiconductors of
81 the indolocarbazole family have similar nitrogen-containing basic units and tend to have
82 a π - π stacking and band gaps between 2.50 and 2.90 eV, depending on the side chains
83 and the oligomer type [21-23]. Their degree of crystallinity has been shown to depend
84 largely on the side chains and oligomer length, copolymers, as well as on the deposition
85 method [21,22]. When they are part of large polymers, they tend to be more amorphous
86 and the diffraction peaks become much broader and can be considerably shifted [23]. An
87 example of these basic semiconductors is shown in Fig. 1, where R can be a side chain.

88

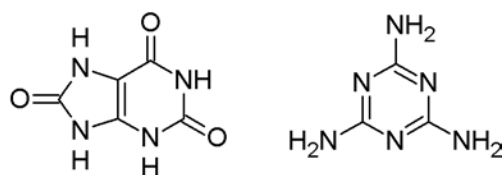


89

90 **Fig. 1.** Chemical structure of based oligomers, R is a side chain [22].

91

92 The specific combination of imidazolic, pyridinic, and graphitic nitrogen of the
93 materials synthesized with UA is actually determined by the decomposition pathway of
94 the crystalline UA and can be regarded as one of the upper limits of nitrogen-doped
95 graphite (graphene) materials, such as those reported by Fechler *et al.* and Mahmood *et*
96 *al.* [17,19].



97

98

Fig. 2. Formulas of uric acid (left) and melamine (right).

99

100 **2. Experimental**

101 **2.1. Materials**

102 Uric acid was supplied by Aesar and melamine was supplied by Sigma-Aldrich with
103 purities higher than 99% (the chemical formulas are displayed in Fig.2). A mixture of 95
104 wt% of uric acid and 5 wt% of melamine was prepared and milled in an agate mortar for
105 5 min (both materials are solids). Portions of 5 g of the blend were treated at different
106 temperatures and times in air: 450 °C for 15 min, 550 °C for 15 min, 600 °C for 15 and
107 30 min. Samples were identified as CN450, CN550, CN600-1, CN600-2, respectively.
108 The (weight) reaction yields were 74.33%, 67.87%, 44.89%, and 34.36%, respectively,
109 corresponding to different decomposition advancements and to the formation of
110 nitrogen-rich powder products. The products exhibited different colors from brown
111 (CN450) to intense black (CN600-2).

112

113 **2.2. Analytical Methods**

114 *FT-IR spectroscopy:* The infrared spectra were obtained by means of a Agilent Carey
115 630 Fourier Transform-Infrared (FT-IR) spectrometer (Agilent Technologies, Santa
116 Clara, CA, USA). The IR spectra were obtained directly from the solid materials by
117 attenuated total reflectance (ATR).

118 *X-ray diffraction measurements:* The X-ray diffraction patterns were obtained with a
119 Rigaku ULTIMA-IV Bragg-Brentano powder diffractometer (Rigaku Corp., Tokyo,

120 Japan) with Cu K α radiation. Glass capillaries were used for sample mounting. The
121 measurements always lasted for 1 hour, and crystalline silicon was used as a standard.

122 *TEM characterization:* Samples were studied by transmission electron microscopy
123 (TEM) with a JEM-2010F and a JEM-1010 (JEOL, Akishima, Tokyo, Japan) in order to
124 observe the particles morphology at lower magnifications and to find structural
125 information complementary to the X-ray diffraction data. The samples' preparation
126 consisted of dispersing the materials into 2-butanol, treating them in an ultrasonic bath
127 for 30 min, and then depositing a micro-droplet (2.5 μ l) of the suspended fraction on a
128 Cu grid. Once the 2-butanol was evaporated, the grids were ready for observation.

129 *Thermal analysis:* The thermal stability and decomposition rate of the products was
130 evaluated by thermogravimetric analysis using a SETSYS Evolution 1750 TGA-
131 DTA/DSC (SETARAM Instrumentation, Caluire-et-Cuire, France) with an nitrogen
132 flow rate of 30 mL/min and a temperature increment rate of 10 $^{\circ}$ C/min up to 900 $^{\circ}$ C.

133 *UV-vis spectroscopy:* UV-Vis diffuse reflectance spectra were measured using a
134 Perkin Elmer Lambda 35 UV-Vis spectrophotometer (Perkin Elmer Inc., Waltham, MA,
135 USA). A Spectralon[®] blank was used as reference. The reflectance data were
136 transformed to absorbance data applying the Kubelka-Munk method (Equation 1):

$$137 \quad F(R) = \frac{(1-R)^2}{2R} \quad (1)$$

138 where R is the reflectance and $F(R)$ is the Kubelka-Munk (K-M) function. The band gap
139 was estimated through a Tauc plot [24,25].

140 *TeraHertz-time domain spectroscopy measurements:* The materials under study were
141 dispersed in polyethylene (PE) powder in a variable low concentration and the mixture
142 was thoroughly milled in an agate mortar in order to form a uniform mixture. Ultra-high
143 molecular weight surface-modified, 53–75 μ m particle size PE from Sigma–Aldrich was
144 employed. The resulting samples were pressed, using a Graseby Specac press, to form

145 pellets with a diameter of 13 mm. A Menlo Tera K15 Spectrometer (Menlo Systems
146 GmbH, Planegg, Germany) was used for the THz-TDS analysis. The system was
147 operated in a nitrogen rich atmosphere in order to avoid the signature of water
148 absorption in the recorded samples. In order to reduce the noise, the results from at least
149 twenty consecutive samples and reference measurements were averaged to obtain the
150 spectral data. The material parameters in the spectral range of interest were calculated
151 from the time domain photocurrent traces measured with the spectrometer. These time
152 domain waveforms depend not only on the material data but also on the width of the
153 pellets due to the contributions from multiple reflections at the pellet-air interfaces.
154 Signal processing techniques similar to those described by Duvillaret *et al.* and flat-top
155 windowing of the time-domain data were employed in order to obtain the THz spectra of
156 the materials [26,27].

157 *X-ray photoelectron spectroscopy:* X-ray photoelectron spectroscopy (XPS) analyses
158 were performed using a Versa Probe II X-ray photoelectron spectrometer (Physical
159 Electronics, Chanhassen, MN, USA) with a monochromatic Al K α X-ray source (1486.6
160 eV) and a base pressure of 1×10^{-9} Torr in the analytical chamber. The X-rays were
161 microfocused at the source to give a spot size on the sample of 100 μm in diameter,
162 using the standard-lens mode. The analyzer was run in constant analyzer energy (CAE)
163 mode. Survey and high resolution spectra were collected using analyzer pass energies of
164 120 and 40 eV, respectively. The binding energy at of 284.6 eV of C-C carbon was used
165 as a reference and a starting point for the C1s peak deconvolution. High resolution
166 spectra were deconvoluted using Gaussian–Lorentzian mix function and Shirley-type
167 background subtraction.

168 *Quantum chemistry calculations:* The semiempirical quantum chemistry
169 computations were performed with the PM6 method using the parallel implementation

170 for multi-threaded shared-memory CPUs and massively parallel GPU acceleration of the
171 MOPAC2012 software package. A Fedora Linux server with a 12 cores Intel Xeon
172 processor and a NVIDIA Tesla K20 GPU were used for the computations [28-30].

173

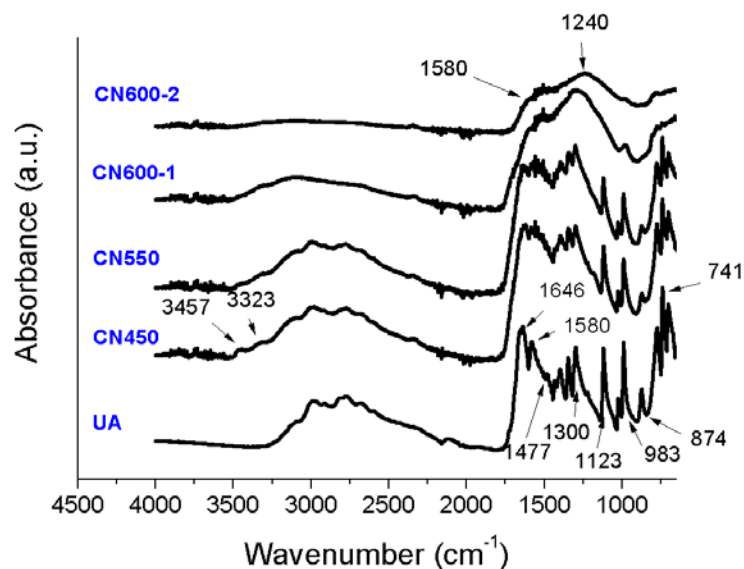
174 **3. Results and discussion**

175 **3.1. Structural and physical-chemical characterization**

176 *3.1.1. Infrared spectroscopy*

177 The IR spectrum of solid UA (see Fig. 2) was dominated by the absorptions related to
178 three chemical groups: NH, OH, and carbonyl CO. The amidic carbonyl generates two
179 bands at 1650 and 1580 cm^{-1} , typical of secondary amides; the band at 1477 cm^{-1} can be
180 related to C-OH bending; and the broad band at around 3000 cm^{-1} is connected to OH
181 stretching vibrations, all interacting by hydrogen bond. The observation of vibrations
182 associated with OH, instead of only CO, is due to imide-amide tautomerism. The imide
183 form of uric acid would be predominant in this supramolecular solid, held by hydrogen
184 bonds. The series of bands between 1410 and 1300 cm^{-1} can be ascribed to O-H in-plane
185 bending vibrations, while the vibration of out-of-plane bending is located at 680 cm^{-1} .
186 The two main peaks between 1123 and 983 cm^{-1} correspond to C-O stretching vibrations
187 of COH. The peaks at 874 and 780 cm^{-1} are due to N-H bending and N-H wagging,
188 respectively.

189



190

191 **Fig. 2.** IR spectra of uric acid (UA) and its pyrolysis products obtained at 450 °C, 550
 192 °C and 600 °C: CN450, CN550, CN600-1 and CN600-2 (CN600-1: 15 min of treatment,
 193 CN600-2: 30 min of treatment).

194

195 The spectrum of CN450 showed the same bands discussed for the UA starting
 196 material. However, it was possible to notice that some small bands appeared at 3457 and
 197 3323 cm⁻¹. These new bands correspond to OH stretching vibrations not interacting via
 198 hydrogen bond, and so they would be indicative of the beginning of the disaggregation
 199 of the supramolecular network. Moreover, the bands of carbonyl stretching and those of
 200 OH in-plane bending seemed to be overlapped with two new growing broad bands. The
 201 situation for CN550 was similar, since the forming pyrolysis product was mixed with the
 202 initial UA and their bands were still overlapped. This transition phase is supported by
 203 the appearance of free OH stretching vibration from the remaining UA molecules, which
 204 are no longer interacting via hydrogen bond due to the transformation of their UA
 205 neighbors into the pyrolysis products.

206 The situation radically changed in CN600-1 and CN600-2 spectra, in which most
 207 bands associated to OH, CO and NH groups disappeared. In the spectrum of the former,

208 some residual C-OH bands were still present, such as the small peak at around 983 cm⁻¹.
209 A shoulder due to carbonyl stretching could also be discerned above 1600 cm⁻¹. It is
210 worth noting that the stretching bands of non-interacting OH (above 3300 cm⁻¹) were
211 proportionally higher than those of CN450 and CN550 samples, indicating that the
212 pyrolysis process was more advanced. Conversely, in CN600-2 spectrum the OH
213 stretching bands had almost disappeared. The broad bands at 1580 and 1240 cm⁻¹ seem
214 to be associated to vibrations of 6-5 atoms nitrogen-containing rings [I. López Tocón,
215 M.S. Woolley, J.C. Otero, J.I. Marcos “Vibrational spectrum of 3-methyl and 4-
216 methylpyridine” Journal of Molecular Structure 470 (1998) 241-246] [31-32]. Indeed,
217 the band at 1580 cm⁻¹ may belong to ring stretching vibrations from both pyridine-like
218 and imidazole (or pyrrole) -like rings, while the band at 1240 cm⁻¹ can be associated to
219 C-N stretching of imidazole-like rings [S. Gunasekaran , G. Sankari, S. Ponnusamyc,
220 “Vibrational spectral investigation on xanthine and its derivatives—theophylline,
221 caffeine and theobromine”, Spectrochimica Acta Part A 61 (2005) 117–127]. This latter
222 claim is also supported by the similarity of the spectrum of CN600-2 to that of nitrogen-
223 doped graphene, where pyrrole-like and pyridine-like nitrogen atoms are present, apart
224 from graphitic nitrogen [31-33].

225

226 3.1.2. *Morphology of the products: TEM analysis*

227 TEM micrographs, representative of the suspended fraction (see Section 2.2) of each of
228 the pyrolysis products, are depicted in Fig. 3.

229

230 **Fig. 3.** TEM micrographs of CN450, CN550, CN600-1 and CN600-2.

231

232 It is noteworthy that the morphology of CN450, with crumpled particles, was similar
233 to that observed in the formation of g-C₃N₄ from melamine cyanurate, which occurs
234 through a topotactic transformation [34]. In CN550 and CN600-1 samples the particles
235 were mainly composed of nanosheets, while in CN600-2 these nanosheets tended to
236 form also hollow structures, as a consequence of the topotactic transformation
237 advancement. As regards CN600-2 sample, it was possible to observe diffraction planes
238 (see Fig. 4). The interplanar distance, 3.36 Å, was found to be compatible with the main
239 peak in the XRD pattern.

240

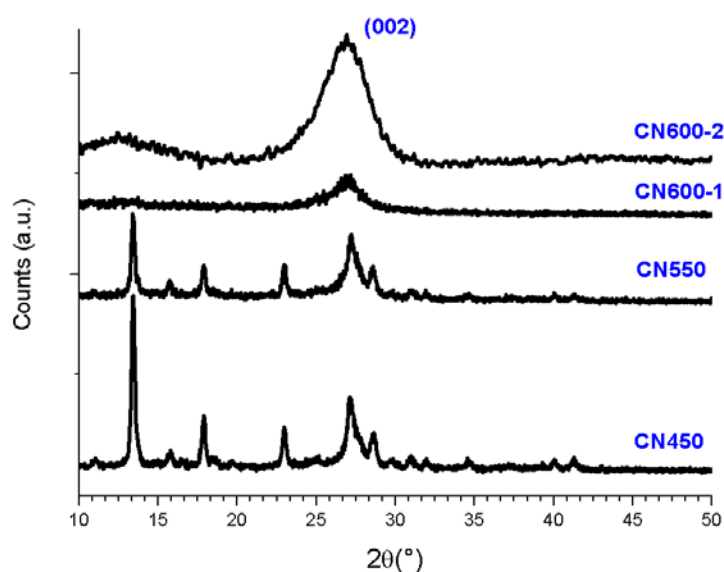
241 **Fig. 4.** Diffraction planes in TEM micrographs of CN600-2 sample. Left: a view on a
242 particle showing an ordered spot in the middle of a more disordered area; Right: an
243 insight view on the ordered spot.

244

245 3.1.3. *X-ray diffraction (XRD) measurements*

246 The powder X-ray diffraction patterns of CN450 and CN550 samples, shown in Fig. 5,
247 were in agreement with that of crystalline UA. This further supports that the starting
248 material (UA) would be still present in considerable amounts in samples treated below
249 600 °C (the XRD pattern of CN450 is substantially identical to that of anhydrous uric
250 acid) [Supplementary Information, Yuya Oaki, Soichiro Kanekoa and Hiroaki Imai,
251 Morphology and orientation control of guanine crystals: a biogenic architecture and its
252 structure mimetics, *J. Mater. Chem.*, 2012,22, 22686-22691]. Moreover, the XRD
253 pattern of CN600-1 corresponded to a quite amorphous material with a broad peak
254 around 27°, which seems to result directly from the UA peak at 27°, provided that the
255 basic layered features of the original structure would be preserved (topotactic
256 transformation). Nevertheless, all the other peaks were not visible. The intensity of the
257 reflection at 26.97°, corresponding to an interplanar spacing of 3.31 Å, became much

258 higher (26.97°), still remaining quite broad, and the broad peak at 12.58° (spacing of
259 7.03 \AA), corresponding to an in-plane structural packing motif, became more evident. It
260 should be pointed out that in the final product the stacking order seems to prevail over
261 the in-plane one. The crystallization process driven by temperature was also revealed by
262 the broad exothermic band found in differential scanning calorimetry at *ca.* 600°C .
263



264

265 **Fig. 5.** X-ray diffraction patterns of CN450, CN550, CN600-1, and CN600-2.

266

267 The typical diffraction peak at around 27° has also been found in other nitrogen-
268 doped graphene or graphite materials. In fact, Horibe *et al.* reported that this interplanar
269 distance decreases monotonously with increasing N/C content ratio [35,36]. According
270 to Horibe's reports, an interplanar distance of 3.31 \AA would correspond to an N/C
271 atomic ratio close to 0.6, which is actually very close to the one found by X-ray
272 photoelectron spectroscopy for the materials under study.

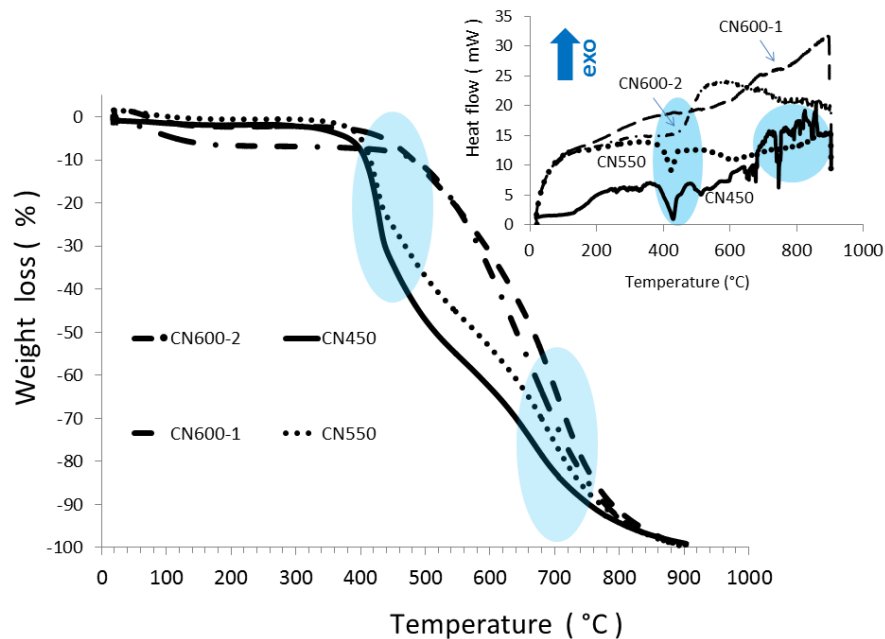
273

274 3.1.4. *Thermal behavior analysis*

275 The weight losses in the thermogravimetric analysis (TGA) curves of both CN450 and
276 CN550 samples (see Fig. 6) in nitrogen atmosphere above 400 °C can be ascribed to UA
277 and melamine decomposition. The loss at around 400 °C (first circle in the TGA
278 thermograms in Fig. 6) was more pronounced in CN450 than in CN550 because of the
279 higher starting material concentration in the former (in which polycondensation was
280 conducted at a lower temperature). These losses were no longer present in CN600-1 and
281 CN600-2 samples, indicating that in the both cases UA had been completely consumed.
282 The second weight loss above 600 °C (second circle in Fig. 6) in all samples was due to
283 the final decomposition of the products.

284 The endothermic peaks in the differential thermal calorimetry (DSC) curves of both
285 CN450 and CN550 (see inset in Fig. 6) at around 400 °C can thus be associated to the
286 starting materials' decomposition. Other DSC peaks above 600 °C may be due to the
287 decomposition of by-products in CN450. The endothermic peaks around 400 °C were no
288 longer present in CN600-1 and CN600-2. On the contrary, broad exothermic peaks at
289 around 600 °C appeared in both CN600-1 and CN600-2 (especially evident in CN600-
290 2). It seems that, in conjunction with the final (endothermic) decomposition, a
291 (exothermic) process of crystallization occurred. These processes were eventually
292 confirmed by X-ray diffraction.

293



294

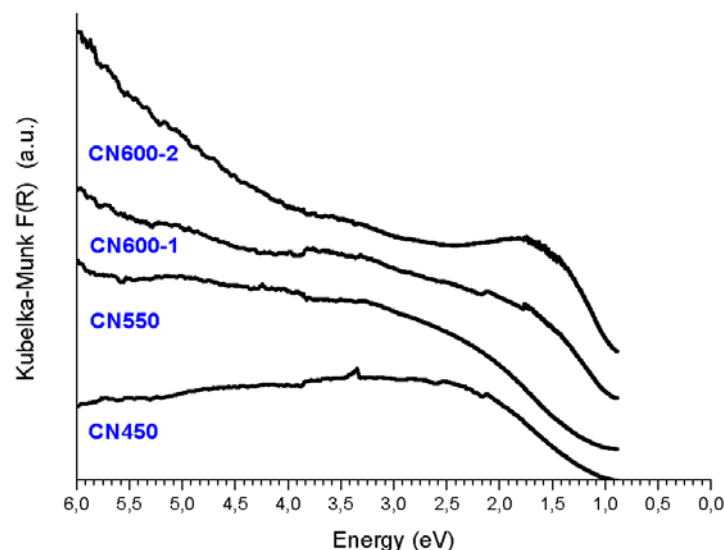
295 **Fig. 6.** Thermogravimetric curves of CN450, CN550, CN600-1, and CN600-2. *Inset:*
 296 differential scanning calorimetry curves of the same samples. The circles in the graphics
 297 highlight the main transformations.

298

299 3.1.5. UV-visible spectroscopy

300 The UV-visible spectra of the four samples exhibited an increase in the absorption as the
 301 polycondensation temperature was increased, as shown in Fig. 7. In the spectrum of
 302 CN600-2 there was an evident but broad peak between 1.7 and 1.5 eV (around the
 303 wavelength of 750 nm) in the red region. The increment in this band intensity would
 304 correspond to the enrichment of the samples in final product as a function of the thermal
 305 treatment temperature, also confirmed by other techniques.

306



307

308 **Fig. 7.** UV-visible Kubelka-Munk, $F(R)$, spectra of CN450, CN550, CN600-1, and
 309 CN600-2.

310

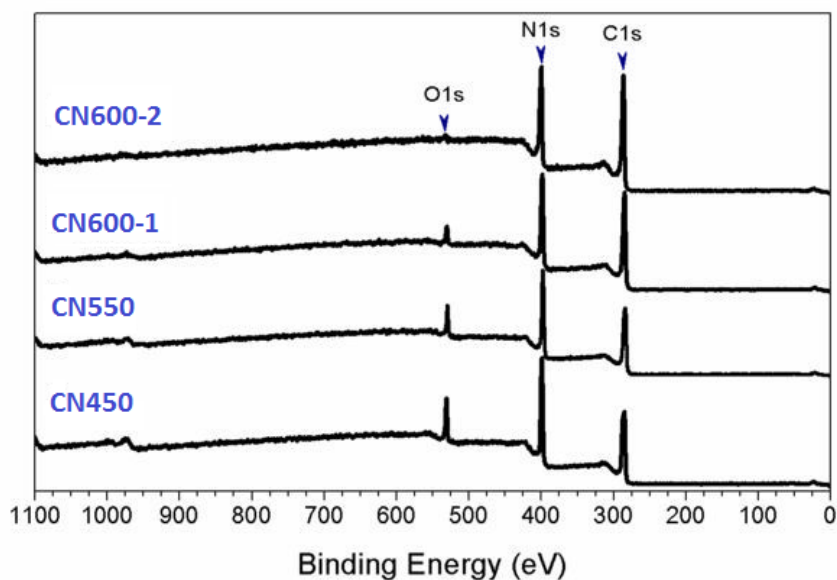
311 The direct band gap values estimated by Tauc plot were 2.10, 2.22 and 2.32 eV for
 312 CN550, CN600-1 and CN600-2, respectively. The direct band gap could not be
 313 determined by Tauc plot for CN450, since the final product yield was still low in this
 314 case. Moreover, the indirect band gap was considerably lower and had values around
 315 0.90 eV for all the samples, indicating that this gap is more related to the assembly of the
 316 product molecules.

317

318 3.1.6. *X-ray photoelectron spectroscopy*

319 In order to confirm the incorporation of nitrogen atoms into the polymer network and to
 320 identify the carbon-nitrogen species formed during the synthesis process, XPS analysis
 321 of the four semiconducting polymer samples was conducted. The evolution and
 322 quantification of the carbon, nitrogen and oxygen species was established by comparison
 323 of the relative intensities of the C1s, N1s and O1s peaks (Fig. 8) and by elemental
 324 quantification of the carbon, nitrogen and oxygen contents (Table 1).

325
 326
 327
 328
 329
 330
 331
 332
 333
 334



335 **Fig. 8.** XPS survey spectra of the samples CN450, CN550, CN600-1, and CN600-2.

336
 337
 338

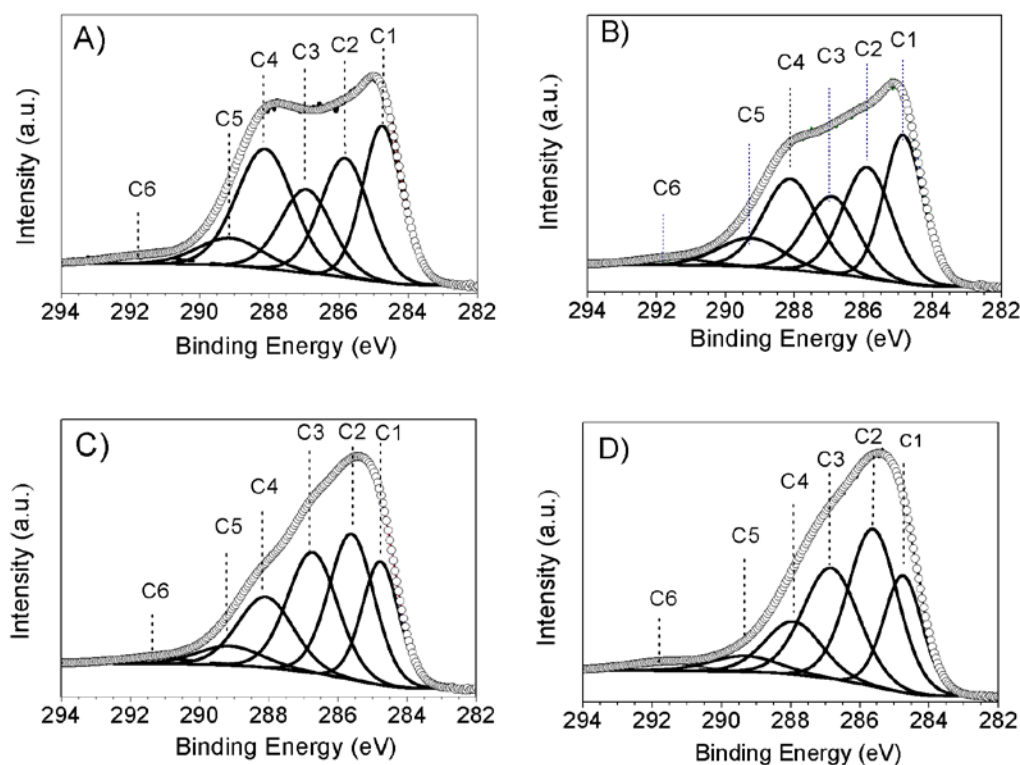
339 **Table 1.** Estimated elemental carbon, nitrogen and oxygen contents for the different UA
 340 polycondensation products.

Sample	C [%]	N [%]	O [%]
CN450	52.4	36.1	11.5
CN550	55.3	34.4	10.3
CN600-1	56.3	36.7	7.0
CN600-2	58.2	37.4	4.4

341
 342
 343
 344
 345

The high-resolution XPS spectra in the C1s region of the four samples are shown in Fig. 9. The spectra were fitted by six Gaussian-Lorentzian contributions with binding energies (BE) centered at 284.8, 285.8, 286.9, 288.1, 289.1 and 291.6 ±0.2 eV, and corresponding to C-C and sp² (C=C) (C1), pyridinic (naphthyridinic) C-N (C2), C=O

346 and imidazolic C-N-H (C3), -COOH and imidazolic C=N (C4), O-C(=O)-O (C5) and π -
 347 π^* (C6), respectively [37-43]. The binding energies and relative weight percent (wt%)
 348 associated with each contribution are summarized in Table 2.
 349



350
 351 **Fig. 9.** High-resolution XPS spectra in the C1s region: deconvoluted peaks for the
 352 various UA polycondensation products: A) CN450, B) CN550, C) CN600-1 and D)
 353 CN600-2.

354
 355 **Table 2.** Deconvolution and carbon chemical species quantification results for C1s core
 356 level spectra (BE: binding energies).

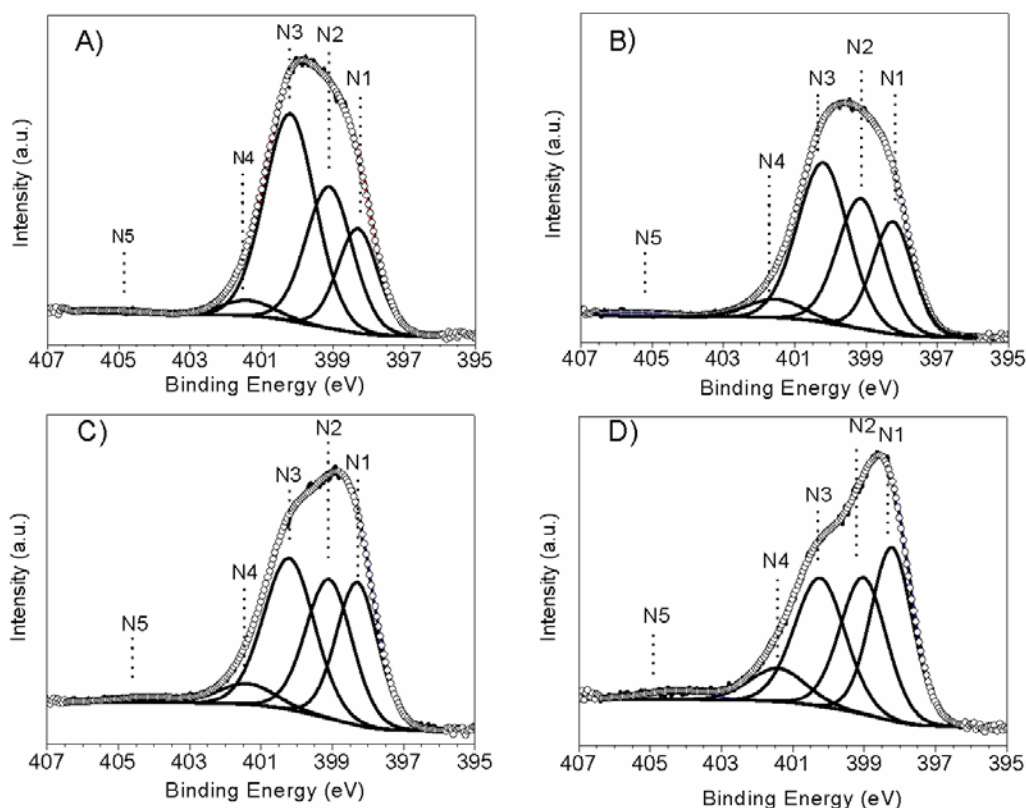
Sample		C1	C2	C3	C4	C5	C6
BE	BE [± 0.2 eV]	284.8	285.8	286.9	288.1	289.1	291.6
CN450	wt%	24.2	22.8	16.9	26.8	7.1	2.3
CN550	wt%	25.8	24.4	17.6	21.9	8.3	2.1
CN600-1	wt%	20.0	29.0	26.6	17.2	5.5	1.9
CN600-2	wt%	19.5	33.8	26.7	12.9	4.7	2.4

357

358 The presence of five nitrogen species in the N1s region, 395.0–407.0 eV, was verified
359 upon deconvolution of the high-resolution spectra of the four samples under study (see
360 Fig. 10). The BEs of the five Gaussian-Lorentzian contributions (*viz.* 398.3, 399.1, 400.2
361 and 404.2 ±0.2 eV), corresponding to pyridinic (naphthyridinic) N (N1), imidazolic C-
362 NH (N2) (a small part of N2 can be also due to nitrile species since a very weak peak
363 can be seen in the IR spectrum of CN600-2), imidazolic C-N-C (N3), graphitic N (with
364 latitude it means a 3-coordinated N similar to that of amorphous CN_x) or C-O-N (N4)
365 and π - π^* (N5), respectively [36-42], and relative weight percent (wt%) values are
366 presented in Table 3.

367 The ratio N1:N2:N3 for CN600-2 was approximately 1:1:1, suggesting that these
368 types of nitrogen could belong to a well-defined structure (not randomly distributed). It
369 is noteworthy that imidazole seems to be formed before than naphthyridine (in fact, the
370 N2 and N3 contents were higher than those of N1 in the samples treated below 600°C),
371 which implies the condensation of the 6 atoms-rings of two UA molecules.

372



373

374 **Fig. 10.** High-resolution XPS spectra in the N1s region: deconvoluted peaks for the
 375 various UA polycondensation products: A) CN450, B) CN550, C) CN600-1 and D)
 376 CN600-2.

377

378

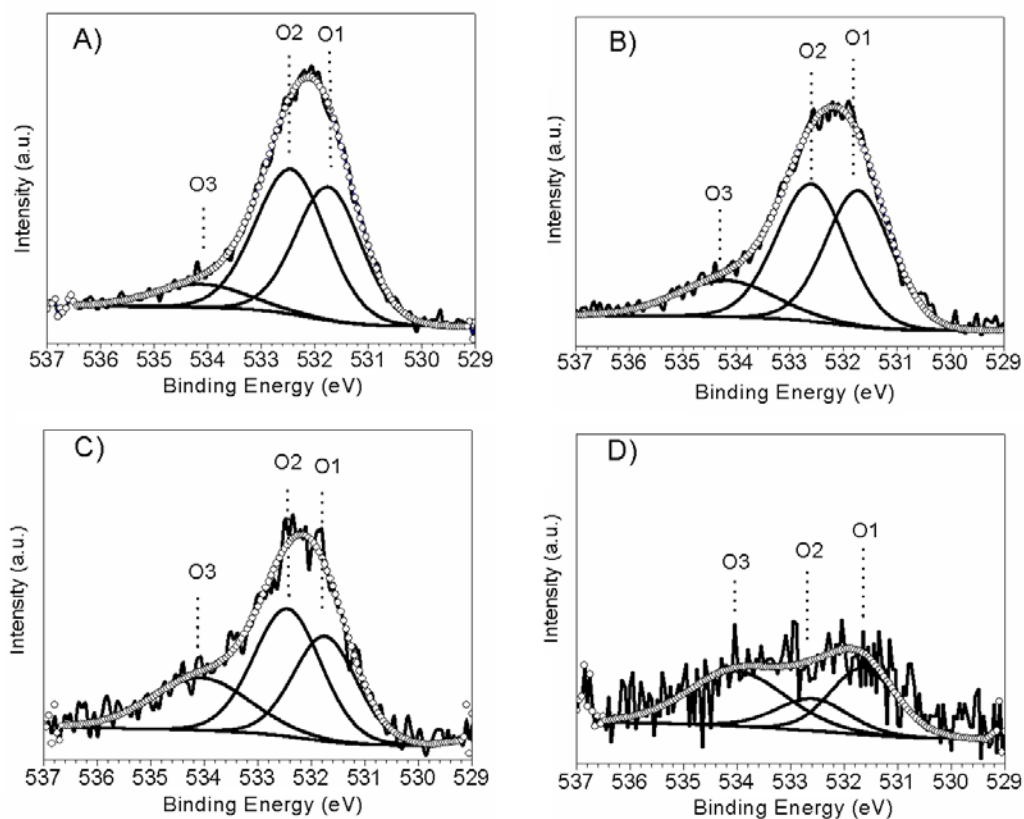
379 **Table 3.** Deconvolution and nitrogen chemical species quantification results for N1s
 380 core level spectra (a) BE was 404.2 eV for both CN600-1 and CN600-2.

Sample		N1	N2	N3	N4	N5
BE	BE [± 0.2 eV]	398.3	399.1	400.2	401.4	405.0
CN450	wt%	19.0	29.4	47.0	3.8	0.8
CN550	wt%	22.8	30.2	40.5	5.3	1.3
CN600-1	wt%	27.6	29.8	35.5	5.4	1.7(a)
CN600-2	wt%	31.9	28.2	28.9	8.4	2.6(a)

381

382 The O1s peaks (in the 529.0–537.0 eV region), arising from the oxygen-carbon
 383 species or from water absorbed on the surface of the semiconductor polymers, are
 384 depicted in Fig. 11, together with their fit to three Gaussian-Lorentzian contributions.

385 These contributions, centered at 531.8, 532.5 and 534.2 ± 0.2 eV, were correlated with
 386 N-C-O (O1), C-O or C-OH (O2) and adsorbed H₂O (O3), respectively. The oxygen
 387 bonds and their relative mass fractions (wt%) are condensed in Table 4.
 388



389
 390 **Fig. 11.** High-resolution XPS spectra in the O1s region: deconvoluted peaks for the
 391 various UA polycondensation products: A) CN450, B) CN550, C) CN600-1 and D)
 392 CN600-2.

393

394 **Table 4.** Deconvolution and oxygen chemical species quantification results for O1s core
 395 level spectra (BE: binding energies).

Sample		O1	O2	O3
BE	BE [± 0.2 eV]	531.8	532.5	534.1
CN450	wt%	41.2	48.6	10.3
CN550	wt%	40.3	43.4	16.3
CN600-1	wt%	32.5	42.3	25.2
CN600-2	wt%	36.3	19.3	44.5

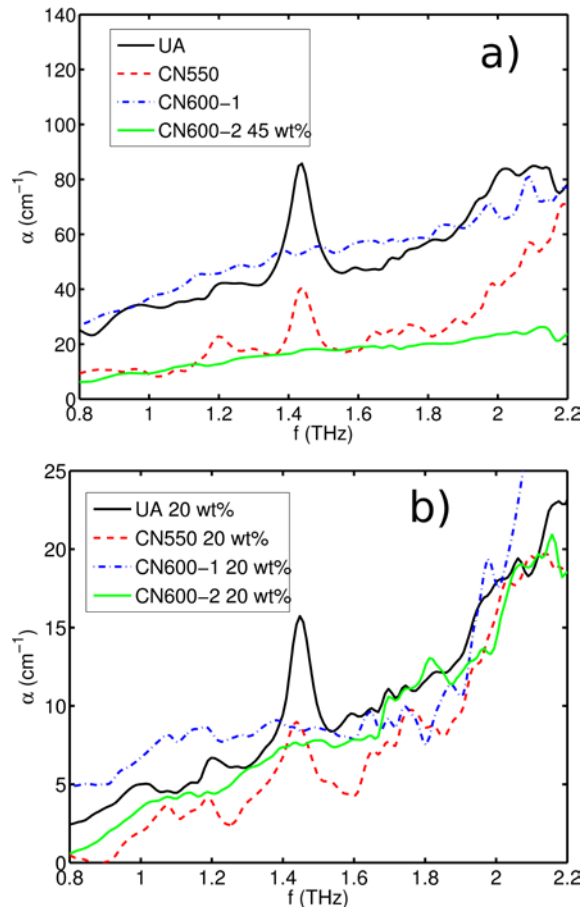
396

397 2.1.7. THz-TDS measurements

398 The room temperature THz-TDS spectra of the four pyrolysis products in the 0.8–2.2
399 THz range are shown in Fig. 12(a) displays the results for pure material pellets –except
400 for CN600-2, which was diluted at a 45 wt% concentration in a PE matrix (since it was
401 impossible to prepare a pure sample pellet)–, while Fig. 12(b) shows the spectra for all
402 the samples dispersed in PE at a 20 wt% concentration. Even though the total absorption
403 was much smaller in this case, which made the measurements noisier, it provided a fair
404 comparison between all the samples.

405 Previously reported THz-TDS measurements of UA at 77 K showed two peaks in this
406 band: a very strong resonance close to 1.5 THz and a much smaller peak near 1.35 THz
407 [44]. Both peaks were clearly present in the UA and CN550 samples, in particular the
408 strongest absorption band, albeit with a red-shift of both resonances, as they were
409 measured at room temperature. This temperature dependence is typical of THz
410 vibrational resonances associated with crystal lattice modes [45]. In the present case, the
411 main signature of the THz spectrum was shifted to 1.44 THz when the measurement was
412 performed at room temperature. A contribution to the total attenuation –that increased
413 monotonically with frequency– was present, which would be due to scattering. There
414 was also a small absorption band at 1.99 THz, which can be due to the presence of
415 melamine at a small concentration [46].

416



417

418 **Fig. 12.** THz-TDS measurements of the samples. The results in (a) correspond to pure
 419 samples, except for CN600-2, for which a pellet in a PE matrix with 45 wt% was used.
 420 In (b), all the samples were dispersed at a 20 wt% concentration in PE.

421

422 The significant reduction of the signature contributed by the precursor material to the
 423 total attenuation after thermal treatment at 550 °C indicates its transformation into the
 424 carbon-nitrogen product. When the processing temperature was further increased to 600
 425 °C, the attenuation traces of the reagent completely disappeared and the attenuation
 426 features typical of disordered materials dominated [47]. There was a reduction of the
 427 total attenuation of CN600-2 when compared to that of CN600-1. Also, the faint
 428 resonance in the higher frequency end of the spectrum that was common to the CN550
 429 and CN600-1 samples vanished in CN600-2. In spite of the fact that the observed
 430 spectral peak was very weak, the THz spectra can be interpreted as an effect of the initial

431 production of the 2D polymer, supporting its presence at an appreciable concentration in
432 CN550 and CN600-1 samples. This conformation has a lattice mode that has been
433 calculated at 2.28 THz and a stronger resonance at 3.23 THz (see below). The presence
434 of this type of lattice resonances in a disordered material can contribute to the generation
435 of a broad spectral feature similar to that observed in CN600-1, and the reduction of the
436 attenuation can indicate a progressive condensation of the material into the 3D phase
437 (stacking of layers) [48]. A similar transition has also been previously explained for g-
438 C₃N₄ on the basis of THz-TDS measurements [49].

439

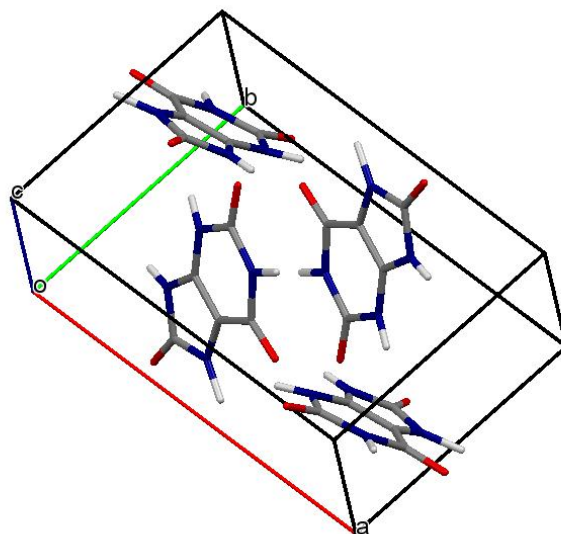
440 **3.2. Semi-empirical quantum chemistry calculations**

441 3.2.1. *Geometry optimization*

442 Uric acid crystals are monoclinic with four molecules in a unit cell (Fig. **13**), with
443 parameters $a=14.464$ Å, $b=7.403$ Å, $c=6.208$ Å, $\beta=65.10^\circ$ [50]. The crystal geometry
444 was optimized with these parameters as the initial conditions using the PM6 method and
445 periodic boundary conditions. The computational period spanned $1\times 2\times 3$ crystal unit
446 cells in the a , b , and c directions, respectively, in order to fulfill the accuracy
447 requirements of MOPAC calculations [51].

448 The crystal parameters of the geometry optimized with the PM6 Hamiltonian were
449 $a=14.870$ Å, $b=7.307$ Å, $c=6.401$ Å, $\alpha=89.76^\circ$, $\beta=64.67^\circ$ and $\gamma=89.78^\circ$, very close to
450 their actual values. In these conditions, it can be expected that the vibrations predicted in
451 the THz range will be close to those of the measured data [45,52].

452

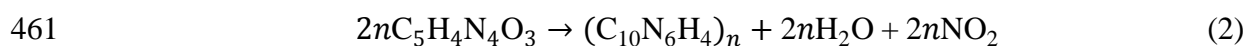


453

454 **Fig. 13.** Unit cell of uric acid.

455

456 Fig. 14 shows the optimized geometry corresponding to the new carbon-nitrogen,
 457 consistent with the observed elemental ratio by XPS. It consists of an alternating
 458 sequence of imidazole and naphthyridine units resulting in a material with an average
 459 formula of $C_5N_3H_2$ (with atomic ratio of nitrogen to carbon of 0.6), which would be
 460 formed by condensation of uric acid molecules, as indicated in Equation 2:

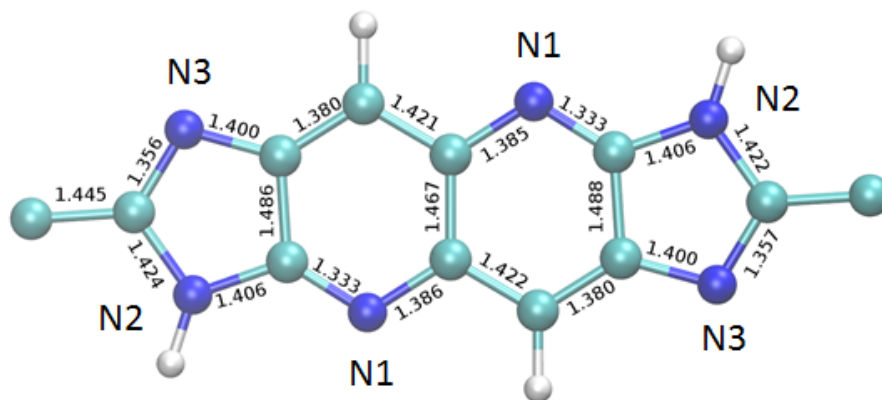


462 In the polymer unit, shown in Fig. 14, the ratio of N1:N2:N3 is 1:1:1, as determined
 463 by XPS. The experimental ratio of N to C of 0.64 for the CN600-2 product, as
 464 determined by XPS, could be ascribed to the presence of a certain amount of graphitic
 465 nitrogen (a nitrogen bonded to three carbon atoms in the naphthenic ring) as a defect in
 466 the polymer chain with three N atoms in the naphthenic rings. Indeed, the N to C ratio
 467 becomes 0.6 when such graphitic nitrogen is neglected.

468 The calculations were performed with the PM6 Hamiltonian and periodic boundary
469 conditions using MOPAC. The length of the polymer repeat unit was $a=10.353 \text{ \AA}$. In
470 spite of the large polarity of imidazole, the symmetric combination of two constituents
471 of this type in the polymer repeat unit permits to cancel out the dipole moment. PM6
472 calculations using MOPAC assign a dipole moment of 4.083 D and $2.772 \times 10^{-3} \text{ D}$ to the
473 imidazole molecule and to the monomer of the carbon-nitrogen system, respectively.

474 Fig. 15 shows the resulting geometry for a 2D polymer obtained by the arrangement
475 of linear chains linked by hydrogen bonds, in a similar fashion to those linking the linear
476 polymer chains in the 2D melon system [49]. The lattice parameters for the 2D polymer
477 were $a=10.360 \text{ \AA}$, $b=6.251 \text{ \AA}$ and $\gamma=89.25^\circ$. Both the 1D and 2D polymers would have a
478 very good planarity.

479

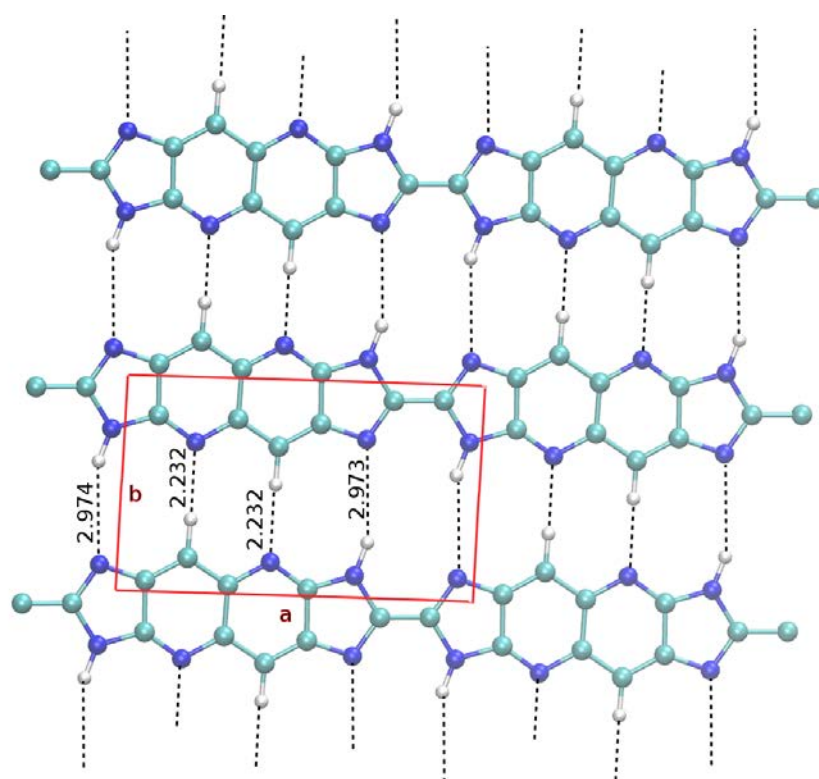


480

481 **Fig. 14.** Optimized geometry for the 1D polymer using the PM6 Hamiltonian. Bond
482 lengths (in Å) are labeled in the figure. N1, N2, and N3 correspond to the nitrogen types
483 identified by XPS. The N1:N2:N3 ratio is 1:1:1, as determined by XPS.

484

485



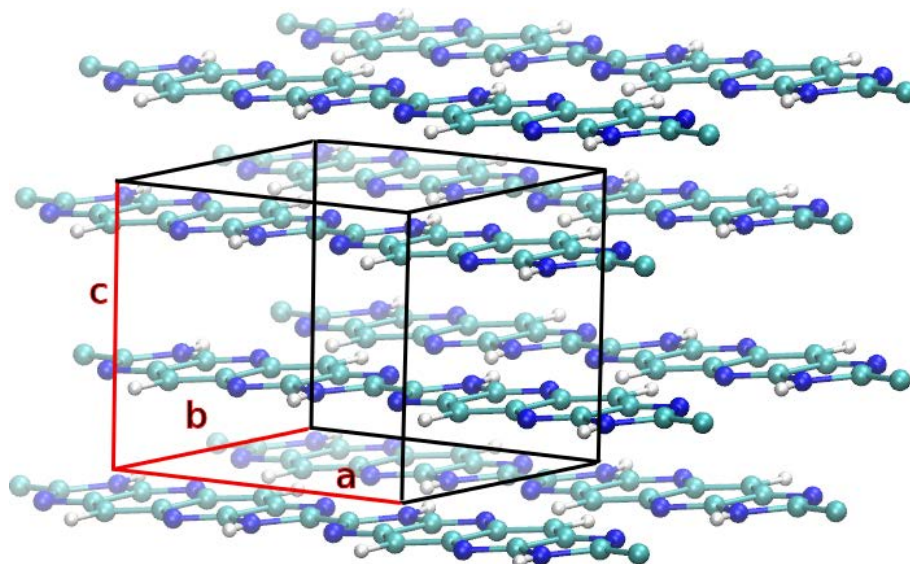
486

487 **Fig. 15.** Optimized geometry for the 2D polymer using the PM6 Hamiltonian. Hydrogen
488 bonds linking the 1D chains are shown with dotted lines. Interatomic distances are in Å.

489

490 The optimized geometry of the 3D crystal obtained with the PM6 method is shown in
491 Fig. 16. The corresponding lattice parameters were $a=10.358$ Å, $b=6.280$ Å, $c=6.928$ Å,
492 $\alpha=85.09^\circ$, $\beta=93.69^\circ$ and $\gamma=89.61^\circ$. The comparison of these results with those of the 2D
493 geometry shows that the 3D geometry would be constituted by piled-up 2D polymer
494 layers which would remain essentially undistorted. The inter-layer distance would be
495 $d=3.451$ Å, in reasonable agreement with the experimental value.

496



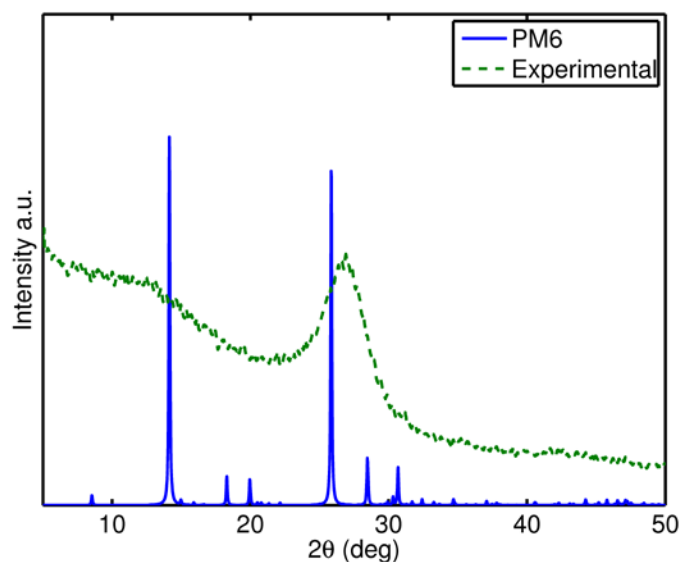
497

498 **Fig. 16.** Optimized geometry for the 3D arrangement obtained from the stacking of 2D
499 polymer layers using the PM6 Hamiltonian.

500

501 The comparison of the XRD pattern simulated from the PM6 geometry with that
502 experimentally measured for CN600-2, using Mercury software, is shown in Fig. 17
503 [51]. There is a small shift of the peak at $2\theta=25.84^\circ$ due to reflections at consecutive
504 material stacks when compared with the corresponding signal in the XRD measurements
505 that is consistent with the previously calculated value of d . The peak at $2\theta=14.14^\circ$ is also
506 identified in the XRD measurements and can be attributed to reflection at every-other
507 layer. This is a characteristic feature (with varying relative intensity) of related ABAB
508 stacked carbon-nitrogen materials [49].

509



510

511 **Fig. 17.** Simulated X-ray powder diffraction pattern for the geometry optimized with the
 512 PM6 Hamiltonian shown in Fig. 16 (*solid line*) and experimental pattern for CN600-2
 513 sample (*dotted line*).

514

515 The total energies per $C_{10}H_4N_6$ unit of the 1D polymer, 2D polymer and 3D crystal
 516 for the geometries optimized with the PM6 Hamiltonian were -2353.83538 eV, -
 517 2354.07442 eV, and -2354.19016 eV, respectively, thus indicating that the condensation
 518 sequence from the 1D to the 2D and, from there, to the 3D phase would be an
 519 energetically favorable process.

520

521 3.2.2. *Vibrational analysis*

522 As discussed above, the study of periodic structures using MOPAC requires an extended
 523 computational period spanning several crystal cells such that the size is sufficient for an
 524 accurate calculation [52]. This has the effect that the calculated frequencies are not
 525 limited to those fulfilling the condition $k \approx 0$ that permits the conservation of total
 526 momentum in the interaction with photons and that, therefore, are relevant for the
 527 absorption spectrum. Thus, a requirement in the interpretation of the MOPAC

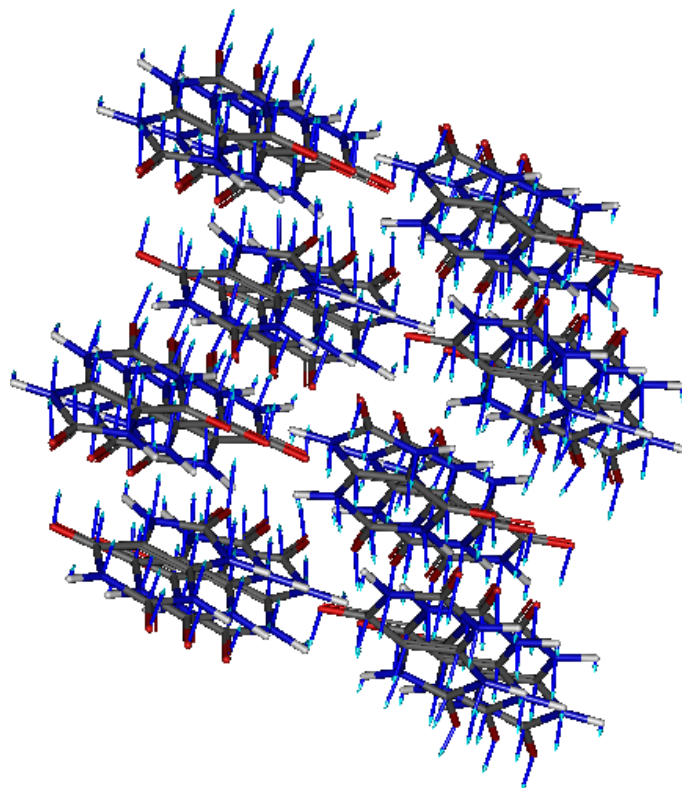
528 calculations of vibration modes in periodic systems is the selection of the relevant
529 vibrations from the whole set of calculated modes [45,53].

530 All the optimized geometries in this study corresponded to true ground states, except
531 for the 3D system depicted in Fig. 16, for which it was not possible to obtain a geometry
532 free from imaginary frequency vibrations.

533 All the plots of displacements of vibration modes were produced with Gabedit [54].
534 In each case, the atomic displacements were scaled to facilitate their visualization.

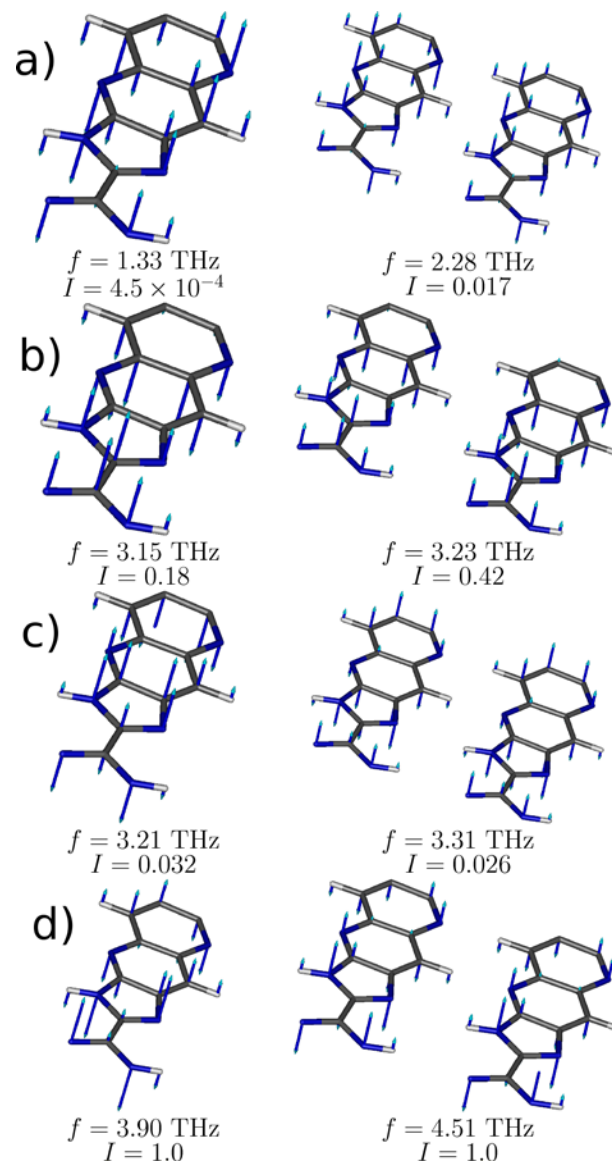
535 The atomic displacements associated to the main resonance of uric acid in the THz
536 band are shown in Fig. 18. This mode was calculated at 1.41 THz, in excellent
537 accordance with the THz-TDS measurements, as expected from the good
538 correspondence between the calculated and experimental crystal parameters.

539



540

541 **Fig. 18.** Atomic displacements for the main vibration mode in the THz band calculated
542 at 1.41 THz with the PM6 method using MOPAC.



544

545 **Fig. 19.** Atomic displacements for the lowest $k=0$ vibration modes of the 1D (left) and
 546 2D (right) polymers. The calculated vibration frequencies f and relative values of
 547 transition dipoles I are annotated in the plot.

548

549 Fig. 19 displays the lowest $k \approx 0$ vibration mode calculated for the 1D (left) and 2D
 550 (right) polymers in the spectral region ranging from 0 up to 6 THz. The side by side
 551 comparison of the plots shows that there exists a direct correspondence between the
 552 vibration modes of the 1D and 2D polymers, even though some differences in the

553 resonance frequencies and relative intensities can be appreciated. The main vibrations in
554 this band correspond to modes b and d in Fig. 19, at 3.15 THz (3.23 THz) and 3.90 THz
555 (4.51 THz) for the 1D (2D) carbon-nitrogen polymer, respectively.

556 As commented above, these vibrations may play a key role in the interpretation of the
557 THz-TDS measurements for labeling the changes in the material morphology for
558 different processing conditions.

559

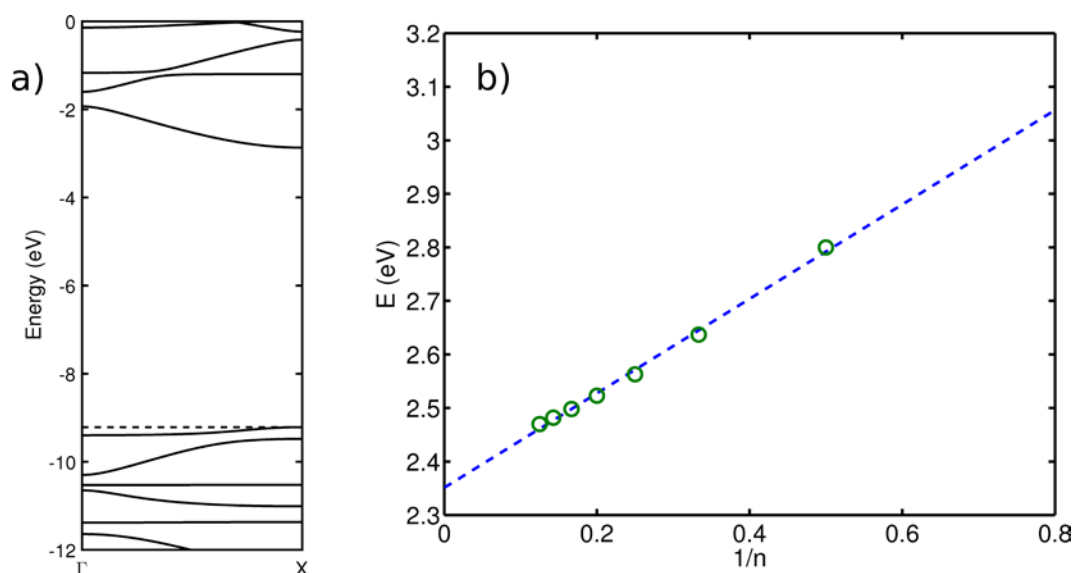
560 3.2.3. *Band gap calculation*

561 Whether a polymer has a direct or indirect band gap can often be predicted from the
562 nodal pseudo-symmetries of the HOMO and LUMO of the constituent monomer at the
563 connecting atomic sites [55]. In this case, such a simple approach is not possible because
564 the monomer HOMO is a non-bonding orbital with nulls at the connecting sites. The
565 electronic band structure calculated using MOPAC, depicted in Fig. 20(a), shows a
566 direct band gap at the edge of the Brillouin zone. Also, the very low dispersive character
567 of the valence band, consistent with the properties of the HOMO, can be appreciated.
568 Besides, the stacking along the *c* axis, can produce the appearance of an indirect band
569 gap in the 3D conformation [55].

570 Even though solid-state MNDO calculations provide a good qualitative description of
571 the band structure of materials, the quantitative estimates of the band gap can be largely
572 biased, in contrast with the high predictive power of vibrational resonances of this type
573 of methods. On the other hand, the bandgap of a polymer can be estimated with good
574 accuracy using the INDO/S with configuration interaction singles (CIS) [56] by the
575 extrapolation of the first excited state obtained for finite size oligomers as the chain
576 length *n* grows [57]. The periodic 1D geometry optimized with the PM6 method
577 implemented in MOPAC was used to generate oligomer geometries of several orders.

578 The energy of the first excited state in each case was calculated using the INDO/S-CIS
579 method, implemented in the ORCA software package [58,59]. The results for the
580 calculated energies for the n -mers are shown in Fig. 20(b) as a function of the inverse
581 chain length $1/n$, together with their corresponding least squares linear fit, which permits
582 to extrapolate the value of E_g as 2.35 eV. This is in very good agreement with the
583 experimental measurements.

584



585

586 **Fig. 20.** (a) Band structure of the 1D polymer calculated using MOPAC. The Fermi level
587 is indicated with a dashed line. (b) Energies for the n -mers calculated with INDO/S-CIS
588 as a function of the inverse chain length $1/n$, together with their corresponding least
589 squares linear fit.

590

591 4. Conclusions

592 A new 2D carbon-nitrogen material was synthesized by pyrolysis of uric acid. The
593 experimental results, obtained through XPS and vibrational spectroscopies, and the
594 quantum chemistry simulations suggest that it would consist of a polymer containing
595 imidazole-like and pyridine (naphthyridine)-like units, held together by a network of

596 hydrogen bonds. This organic semiconductor exhibits characteristics which substantially
597 differ from those of g-C₃N₄, and can be regarded as one of the upper-limit cases of
598 nitrogen-doped graphite (graphene), featuring an atomic ratio of nitrogen to carbon close
599 to 0.6, corresponding to a formula of C₅N₃. The experimental ratio was 0.64 because of
600 the presence of a certain amount of graphitic nitrogen as a defect in the polymer chain.
601 The amount of this type of 3-coordinated nitrogen (possibly belonging to amorphous
602 CN_x species) increased in the samples synthesized at 600 °C, and can be subject of
603 further studies. Its direct optical band gap ranged from 2.10 to 2.32 eV, depending on
604 the polycondensation temperature, very close to the experimental value of 2.35 eV
605 obtained from semiempirical calculations. This band gap is lower than that of g-C₃N₄,
606 allowing this new material to absorb more visible light to be used as a photocatalyst. A
607 good correspondence between experimental and calculated values was also attained for
608 the interplanar distance (*ca.* 3.31 Å), which was consistent with a topotactic
609 transformation, and for the THz-TDS spectroscopy spectra, which showed a behavior
610 similar to that of amorphous 2D carbons, with non-interacting layer planes.

611

612 **References**

- 613 [1] M.L. Cohen, Calculation of bulk moduli of diamond and zinc-blende solids, *Phys.*
614 *Rev. B* 32(12) (1985) 7988-7991.
- 615 [2] A.Y. Liu, M.L. Cohen, Structural properties and electronic structure of low-
616 compressibility materials: β-Si₃N₄ and hypothetical β-C₃N₄, *Phys. Rev. B* 41(15)
617 (1990) 10727-10734.
- 618 [3] X. Li, J. Zhang, L. Shen, Y. Ma, W. Lei, Q. Cui, et al., Preparation and
619 characterization of graphitic carbon nitride through pyrolysis of melamine, *Appl.*
620 *Phys. A* 94(2) (2008) 387-392.

- 621 [4] Y. Zhao, Z. Liu, W. Chu, L. Song, Z. Zhang, D. Yu, et al., Large-Scale Synthesis
622 of Nitrogen-Rich Carbon Nitride Microfibers by Using Graphitic Carbon Nitride
623 as Precursor, *Adv. Mater.* 20(9) (2008) 1777-1781.
- 624 [5] R.C. Dante, J. Martín-Gil, L. Pallavidino, F. Geobaldo, Synthesis under Pressure
625 of Potential Precursors of CN_x Materials Based on Melamine and Phenolic Resins,
626 *J. Macromol. Sci., Part B: Phys.* 49(2) (2010) 371-382.
- 627 [6] G. Zhang, M. Zhang, X. Ye, X. Qiu, S. Lin, X. Wang, Iodine Modified Carbon
628 Nitride Semiconductors as Visible Light Photocatalysts for Hydrogen Evolution,
629 *Adv. Mater.* 26(5) (2014) 805-809.
- 630 [7] J. Zhang, J. Sun, K. Maeda, K. Domen, P. Liu, M. Antonietti, et al., Sulfur-
631 mediated synthesis of carbon nitride: Band-gap engineering and improved
632 functions for photocatalysis, *Energy Environm. Sci.* 4(3) (2011) 675.
- 633 [8] Y. Zhang, X. Bo, A. Nsabimana, C. Luhana, G. Wang, H. Wang, et al., Fabrication
634 of 2D ordered mesoporous carbon nitride and its use as electrochemical sensing
635 platform for H₂O₂, nitrobenzene, and NADH detection, *Biosens. Bioelectron.* 53
636 (2014) 250-256.
- 637 [9] Y. Zhang, T. Mori, J. Ye, Polymeric Carbon Nitrides: Semiconducting Properties
638 and Emerging Applications in Photocatalysis and Photoelectrochemical Energy
639 Conversion, *Sci. Adv. Mater.* 4(2) (2012) 282-291.
- 640 [10] Y. Zhang, Z. Schnepf, J. Cao, S. Ouyang, Y. Li, J. Ye, et al., Biopolymer-
641 Activated Graphitic Carbon Nitride towards a Sustainable Photocathode Material,
642 *Sci. Rep.* 3 (2013).
- 643 [11] A. Vinu, K. Ariga, T. Mori, T. Nakanishi, S. Hishita, D. Golberg, et al.,
644 Preparation and Characterization of Well-Ordered Hexagonal Mesoporous Carbon
645 Nitride, *Adv. Mater.* 17(13) (2005) 1648-1652.

- 646 [12] H. Zhao, M. Lei, X.a. Yang, J. Jian, X. Chen, Route to GaN and VN Assisted by
647 Carbothermal Reduction Process, *J. Am. Chem. Soc.* 127(45) (2005) 15722-
648 15723.
- 649 [13] J.L. Zimmerman, R. Williams, V.N. Khabashesku, J.L. Margrave, Synthesis of
650 Spherical Carbon Nitride Nanostructures, *Nano Lett.* 1(12) (2001) 731-734.
- 651 [14] C. Cao, F. Huang, C. Cao, J. Li, H. Zhu, Synthesis of Carbon Nitride Nanotubes
652 via a Catalytic-Assembly Solvothermal Route, *Chem. Mater.* 16(25) (2004) 5213-
653 5215.
- 654 [15] A. Thomas, A. Fischer, F. Goettmann, M. Antonietti, J.-O. Müller, R. Schlögl, et
655 al., Graphitic carbon nitride materials: variation of structure and morphology and
656 their use as metal-free catalysts, *J. Mater. Chem.* 18(41) (2008) 4893.
- 657 [16] D. Wei, Y. Liu, Y. Wang, H. Zhang, L. Huang, G. Yu, Synthesis of N-Doped
658 Graphene by Chemical Vapor Deposition and Its Electrical Properties, *Nano Lett.*
659 9(5) (2009) 1752-1758.
- 660 [17] J. Mahmood, E.K. Lee, M. Jung, D. Shin, I.-Y. Jeon, S.-M. Jung, et al.,
661 Nitrogenated holey two-dimensional structures, *Nat. Commun.* 6 (2015) 6486.
- 662 [18] H. Wang, X. Li, J. Yang, The g-C₃N₄/C₂N Nanocomposite: A g-C₃N₄-Based
663 Water-Splitting Photocatalyst with Enhanced Energy Efficiency, *ChemPhysChem*
664 17(13) (2016) 2100-2104.
- 665 [19] N. Fechler, N.P. Zussblatt, R. Rothe, R. Schlögl, M.-G. Willinger, B.F. Chmelka,
666 et al., Eutectic Syntheses of Graphitic Carbon with High Pyrazinic Nitrogen
667 Content, *Adv. Mater.* 28(6) (2016) 1287-1294.
- 668 [20] C. Goel, H. Bhunia, P.K. Bajpai, Mesoporous carbon adsorbents from melamine-
669 formaldehyde resin using nanocasting technique for CO₂ adsorption, *J. Environ.*
670 *Sci.* 32 (2015) 238-248.

- 671 [21] Y. Wu, Y. Li, S. Gardner, B.S. Ong, Indolo[3,2-b]carbazole-Based Thin-Film
672 Transistors with High Mobility and Stability, *J. Am. Chem. Soc.* 127(2) (2005)
673 614-618.
- 674 [22] P.-L.T. Boudreault, S. Wakim, N. Blouin, M. Simard, C. Tessier, Y. Tao, et al.,
675 Synthesis, Characterization, and Application of Indolo[3,2-b]carbazole
676 Semiconductors, *J. Am. Chem. Soc.* 129(29) (2007) 9125-9136.
- 677 [23] M. Akimoto, T. Kawano, Y. Iwasawa, Y. Takahashi, K. Yamashita, M.
678 Kawamoto, et al., Syntheses and properties of copolymers containing
679 indolocarbazole moiety in the side chain, *Polym. J.* 43(12) (2011) 959-965.
- 680 [24] J. Tauc, R. Grigorovici, A. Vancu, Optical Properties and Electronic Structure of
681 Amorphous Germanium, *Physica Status Solidi B: Basic Solid State Physics* 15(2)
682 (1966) 627-637.
- 683 [25] J. Tauc, Optical properties and electronic structure of amorphous Ge and Si,
684 *Mater. Res. Bull.* 3(1) (1968) 37-46.
- 685 [26] L. Duvillaret, F. Garet, J.L. Coutaz, A reliable method for extraction of material
686 parameters in terahertz time-domain spectroscopy, *IEEE J. Sel. Top. Quantum*
687 *Electron.* 2(3) (1996) 739-746.
- 688 [27] J. Vázquez-Cabo, P. Chamorro-Posada, F.J. Fraile-Peláez, Ó. Rubiños-López, J.M.
689 López-Santos, P. Martín-Ramos, Windowing of THz time-domain spectroscopy
690 signals: A study based on lactose, *Opt. Commun.* 366 (2016) 386-396.
- 691 [28] J.J.P. Stewart, Optimization of parameters for semiempirical methods V:
692 Modification of NDDO approximations and application to 70 elements, *J. Mol.*
693 *Model.* 13(12) (2007) 1173-1213.
- 694 [29] J.D.C. Maia, G.A. Urquiza Carvalho, C.P. Manguiera, S.R. Santana, L.A.F.
695 Cabral, G.B. Rocha, GPU Linear Algebra Libraries and GPGPU Programming for

696 Accelerating MOPAC Semiempirical Quantum Chemistry Calculations, *J. Chem.*
697 *Theory Comput.* 8(9) (2012) 3072-3081.

698 [30] J.J.P. Stewart, MOPAC2012, Stewart Computational Chemistry, Colorado
699 Springs, CO, USA, 2012.

700 [31] Y. Zhang, Z. Sun, H. Wang, Y. Wang, M. Liang, S. Xue, Nitrogen-doped
701 graphene as a cathode material for dye-sensitized solar cells: effects of
702 hydrothermal reaction and annealing on electrocatalytic performance, *RSC Adv.*
703 5(14) (2015) 10430-10439.

704 [32] S. Indrawirawan, H. Sun, X. Duan, S. Wang, Low temperature combustion
705 synthesis of nitrogen-doped graphene for metal-free catalytic oxidation, *J. Mater.*
706 *Chem. A* 3(7) (2015) 3432-3440.

707 [33] G. Wang, L.-T. Jia, Y. Zhu, B. Hou, D.-B. Li, Y.-H. Sun, Novel preparation of
708 nitrogen-doped graphene in various forms with aqueous ammonia under mild
709 conditions, *RSC Adv.* 2(30) (2012) 11249.

710 [34] J. Liu, H. Wang, M. Antonietti, Graphitic carbon nitride "reloaded": emerging
711 applications beyond (photo)catalysis, *Chem. Soc. Rev.* 45(8) (2016) 2308-2326.

712 [35] L.T. Soo, K.S. Loh, A.B. Mohamad, W.R.W. Daud, The effect of varying N/C
713 ratios of nitrogen precursors during non-metal graphene catalyst synthesis, *Int. J.*
714 *Hydrogen Energy* (2016).

715 [36] T. Horibe, K. Kusaba, K. Niwa, M. Hasegawa, K. Yasuda, R. Ishigami, Molecular
716 routes syntheses of graphite-like C–N compounds with various N/C ratios
717 in high pressure and temperature, *J. Ceram. Soc. Jpn.* 124(10) (2016) 1013-1016.

718 [37] A.P. Dementjev, A. de Graaf, M.C.M. van de Sanden, K.I. Maslakov, A.V.
719 Naumkin, A.A. Serov, X-Ray photoelectron spectroscopy reference data for
720 identification of the C₃N₄ phase in carbon–nitrogen films, *Diamond Relat. Mater.*

721 9(11) (2000) 1904-1907.

722 [38] D. Hulicova-Jurcakova, M. Kodama, S. Shiraishi, H. Hatori, Z.H. Zhu, G.Q. Lu,
723 Nitrogen-Enriched Nonporous Carbon Electrodes with Extraordinary
724 Supercapacitance, *Adv. Funct. Mater.* 19(11) (2009) 1800-1809.

725 [39] S. Kundu, T.C. Nagaiah, W. Xia, Y. Wang, S.V. Dommele, J.H. Bitter, et al.,
726 Electrocatalytic Activity and Stability of Nitrogen-Containing Carbon Nanotubes
727 in the Oxygen Reduction Reaction, *J. Phys. Chem. C* 113(32) (2009) 14302-
728 14310.

729 [40] H. Liu, Y. Zhang, R. Li, X. Sun, S. Désilets, H. Abou-Rachid, et al., Structural and
730 morphological control of aligned nitrogen-doped carbon nanotubes, *Carbon* 48(5)
731 (2010) 1498-1507.

732 [41] A. Kumar, A. Ganguly, P. Papakonstantinou, Thermal stability study of nitrogen
733 functionalities in a graphene network, *J. Phys.: Condens. Matter* 24(23) (2012)
734 235503.

735 [42] T. Sharifi, G. Hu, X. Jia, T. Wågberg, Formation of Active Sites for Oxygen
736 Reduction Reactions by Transformation of Nitrogen Functionalities in Nitrogen-
737 Doped Carbon Nanotubes, *ACS Nano* 6(10) (2012) 8904-8912.

738 [43] M. Scardamaglia, C. Struzzi, S. Osella, N. Reckinger, J.-F. Colomer, L. Petaccia,
739 et al., Tuning nitrogen species to control the charge carrier concentration in highly
740 doped graphene, *2D Materials* 3(1) (2016) 011001.

741 [44] P.C. Upadhyaya, Y.C. Shen, A.G. Davies, E.H. Linfield, *J. Biol. Phys.* 29(2/3)
742 (2003) 117-121.

743 [45] P. Chamorro-Posada, Study of the terahertz spectra of crystalline materials using
744 NDDO semi-empirical methods: polyethylene, poly (vinylidene fluoride) form II
745 and α -D-glucose, arXiv:1604.03919 [physics.chem-ph] (2016).

- 746 [46] M.H. Mingxia He, J.H. Jiaguang Han, M.L. Meng Li, Z.T. Zhen Tian, Y.Y.
747 Yanjun Yu, W.Z. Weili Zhang, Terahertz spectroscopy studies of far-infrared
748 optical and dielectric signatures of melamine, *Chin. Opt. Lett.* 9(s1) (2011)
749 s10507-310509.
- 750 [47] M. Walther, B.M. Fischer, P. Uhd Jepsen, Noncovalent intermolecular forces in
751 polycrystalline and amorphous saccharides in the far infrared, *Chem. Phys.* 288(2-
752 3) (2003) 261-268.
- 753 [48] P. Chamorro-Posada, J. Vázquez-Cabo, Ó. Rubiños-López, J. Martín-Gil, S.
754 Hernández-Navarro, P. Martín-Ramos, et al., THz TDS study of several sp²
755 carbon materials: Graphite, needle coke and graphene oxides, *Carbon* 98 (2016)
756 484-490.
- 757 [49] P. Chamorro-Posada, J. Vázquez-Cabo, F.M. Sánchez-Arévalo, P. Martín-Ramos,
758 J. Martín-Gil, L.M. Navas-Gracia, et al., 2D to 3D transition of polymeric carbon
759 nitride nanosheets, *J. Solid State Chem.* 219 (2014) 232-241.
- 760 [50] H. Ringertz, The molecular and crystal structure of uric acid, *Acta Crystallogr.*
761 20(3) (1966) 397-403.
- 762 [51] C.F. Macrae, P.R. Edgington, P. McCabe, E. Pidcock, G.P. Shields, R. Taylor, et
763 al., Mercury: visualization and analysis of crystal structures, *J. Appl. Crystallogr.*
764 39(3) (2006) 453-457.
- 765 [52] J.J.P. Stewart, Application of the PM6 method to modeling the solid state, *J. Mol.*
766 *Model.* 14(6) (2008) 499-535.
- 767 [53] P. Chamorro-Posada, I. Silva-Castro, J. Vázquez-Cabo, P. Martín-Ramos, J.M.
768 López-Santos, J. Martín-Gil, A Study of the Far Infrared Spectrum of N-Acetyl-D-
769 Glucosamine Using THz-TDS, FTIR, and Semiempirical Quantum Chemistry
770 Methods, *J. Spectrosc.* 2016 (2016) 1-7.

- 771 [54] A.-R. Allouche, Gabedit-A graphical user interface for computational chemistry
772 softwares, *J. Comput. Chem.* 32(1) (2011) 174-182.
- 773 [55] D.-K. Seo, R. Hoffmann, Direct and indirect band gap types in one-dimensional
774 conjugated or stacked organic materials, *Theor. Chem. Acc.* 102(1-6) (1999) 23-
775 32.
- 776 [56] J. Ridley, M. Zerner, An intermediate neglect of differential overlap technique for
777 spectroscopy: Pyrrole and the azines, *Theor. Chim. Acta* 32(2) (1973) 111-134.
- 778 [57] P.M. Lahti, J. Obrzut, F.E. Karasz, Use of the Pariser-Parr-Pople approximation to
779 obtain practically useful predictions for electronic spectral properties of
780 conducting polymers, *Macromolecules* 20(8) (1987) 2023-2026.
- 781 [58] M.C. Zerner, G.H. Loew, R.F. Kirchner, U.T. Mueller-Westerhoff, An
782 intermediate neglect of differential overlap technique for spectroscopy of
783 transition-metal complexes. Ferrocene, *J. Am. Chem. Soc.* 102(2) (1980) 589-599.
- 784 [59] F. Neese, The ORCA program system, *Wiley Interdiscip. Rev.: Comput. Mol. Sci.*
785 2(1) (2012) 73-78.